Directly Assembled 3D Molybdenum Disulfide on Silicon Wafer for Efficient Photoelectrochemical Water Reduction

Dinsefa Mensur Andoshe, Gangtae Jin, Chang-Soo Lee, Changyeon Kim, Ki Chang Kwon, Seokhoon Choi, Woonbae Sohn, Cheon Woo Moon, Seung Hee Lee, Jun Min Suh, Sungwoo Kang, Jaehyun Park, Hoseok Heo, Jong Kyu Kim, Seungwu Han, Moon-Ho Jo, and Ho Won Jang**

MoS_2 composed of earth-abundant elements is considered as a promising hydrogen evolution reaction (HER) catalyst for p-type Si photocathode owing to its appropriate hydrogen adsorption free energy for the edge sites and high photochemical stability in acidic electrolytes. However, the direct synthesis of uniform and atomically thin MoS_2 on Si by usual chemical vapor deposition techniques remains challenging because of the weak van der Waals interaction between Si and MoS_2. Herein, by controlling the gas phase kinetics during metal–organic chemical vapor deposition, wafer-scale direct synthesis of 3D MoS_2 films on TiO_2-coated p-type Si substrates is demonstrated. The 3D MoS_2 layer with a number of edge sites exposed to ambient substantially reduces the HER overpotential of Si photocathode and simultaneously increases the saturation current density due to the antireflection effect. Directly grown 3D MoS_2 thin films are stable under extended water reduction duration. The strategy paves the way for efficient assembly of transition metal disulfide HER catalysts on the p-type photocathode.

1. Introduction

After Fujishima and Honda reported the splitting mechanism of water into its constituent molecule H_2 and $½O_2$ using TiO_2 photoelectrodes, conversion of solar energy to storable chemical fuels became an alternative path for the search of clean energy sources.[1] Therefore, a diverse class of semiconductor photoelectrodes and nonprecious catalytic materials has been investigated for solar water splitting.[2–5] Only a few semiconductor photocathodes and noble metal-free catalysts showed encouraging solar water splitting performances for hydrogen productions.[6–9] Silicon (Si) is an ideal photocathode material with a narrow bandgap ($E_g = 1.12$ eV) with a wide spectral absorption upon solar radiation[10] and appropriate band-edge positions. However, the poor stability in the liquid electrolytes and the high overpotential for charge transfers at the solid/liquid interfaces are yet to be overcome. Furthermore, the charge generation efficiency of Si photocathodes is limited by the high optical reflectance, i.e., 37% (arithmetic mean) of the incident light is reflected in the entire visible range.[11] Therefore, choosing appropriate catalytic materials to mitigate the overpotentials of Si photocathodes is critical to stabilize the liquid electrolyte for the extended operation time and reduce the substantial reflectance of Si for the higher photoelectrochemical (PEC) performance.

Currently, among the noble metal-free catalysts to decrease the overpotential of the p-type Si (p-Si) photocathode for the PEC hydrogen production, molybdenum disulfide (MoS_2) has gained considerable attention as a promising hydrogen evolution reaction (HER) catalyst owing to its low hydrogen adsorption free energy and the high photochemical stability at the affordable expenses, compared to conventional catalysts based on precious metals.[12–15] The transition from the indirect bandgap structures in bulk MoS_2 to the direct bandgap one in MoS_2 monolayers may also improve the charge transport efficiencies.[16,17] There are three main techniques to enhance the catalytic activity of MoS_2 layer.[18–21] First, the phase transition of 2H-MoS_2 to 1T-MoS_2 is effective way to improve the catalytic activity because the 1T-MoS_2 has metallic nature. The 1T-MoS_2 has many catalytic active sites compared to 2H-MoS_2.[18,19] Second, the introduction of sulfur vacancy and strain in MoS_2 is one of promising way to elevate its catalytic activity. By demonstrating the theoretical and experimental results related to

Dr. D. M. Andoshe, C. Kim, K. C. Kwon, S. Choi, W. Sohn, C. W. Moon, J. M. Suh, S. Kang, Prof. S. Han, Prof. H. W. Jang
Department of Materials Science and Engineering
Research Institute of Advanced Materials
Seoul National University
Seoul 08826, Republic of Korea
E-mail: hwjang@snu.ac.kr

G. Jin, C.-S. Lee, J. Park, Dr. H. Heo, Prof. M.-H. Jo
Center for Artificial Low Dimensional Electronic Systems
Institute for Basic Science (IBS)
Pohang 37673, Republic of Korea
E-mail: mhjo@postech.ac.kr

G. Jin, C.-S. Lee, S. H. Lee, J. Park, Dr. H. Heo, Prof. J. K. Kim, Prof. M.-H. Jo
Department of Materials Science and Engineering
Pohang University of Science and Technology (POSTECH)
Pohang 37673, Republic of Korea

The ORCID identification number(s) for the author(s) of this article can be found under https://doi.org/10.1002/adsu.201700142.

DOI: 10.1002/adsu.201700142

the sulfur vacancies and strain in MoS_2, the hydrogen adsorption Gibbs free energy of sulfur vacancy sites is much lower than that of basal plane MoS_2.[20] Furthermore, the strain in MoS_2 layer can help adsorb hydrogen ions on their structure effectively.[21] Finally, the increase of catalytic edges of MoS_2 during its growth steps. The MoS_2 synthesized by chemical vapor deposition (CVD) or metal–organic CVD (MOCVD) should be 2H-MoS_2 because the thermodynamically metastable 1T-MoS_2 would be transformed to 2H-MoS_2 by high growth temperature. Thus, multiplying the exposed edge site density is directly related to developing efficient p-Si photocathodes with MoS_2 HER catalysts.

p-Si is not the best substrate for the direct deposition of atomically thin MoS_2 using the usual vapor deposition techniques because of the weak van der Waals interaction between Si and sulfur (the surface terminating atom in MoS_2).[22,23] To date, most of the MoS_2 films have been deposited on silicon dioxides[24] or sapphires and manually transferred to the p-Si substrates[25–27] to form HER catalysts. However, this manual transfer is not immune from unwanted organic contaminants, and the poor adhesion of transferred MoS_2 layers to the p-Si substrates deteriorates the interfacial charge transport. In addition, the MoS_2 catalyst layers can be easily peeled off from the p-Si photocathode after several tens of hours of hydrogen production. Thus, direct synthesis of MoS_2 catalysts on p-Si substrates is crucial to achieving the efficient solar HER.[28,29] The direct growth of MoS_2 catalysts on p-Si substrate is difficult because of the oxidation of Si substrate and poor adhesion between directly grown MoS_2 and p-Si. The highly crystalline MoS_2 nanosheets or particles could be synthesized onto oxide substrates such as SiO_2 and Al_2O_3.

In this study, we demonstrate the high-PEC performance of Si-based photocathodes by incorporating directly grown 3D MoS_2 HER catalysts with the high density of the exposed edge sites and nanoscale grain boundaries. We utilized the TiO_2 layer as an oxide layer to enhance the nucleation of MoS_2 directly on p-Si substrate and as a passivation layer to inhibit the oxidation of p-Si substrate. The directly grown 3D MoS_2 on TiO_2/p-Si photocathodes achieved a high saturation current density of 37 mA cm^{-2} and a short-circuit current density of 28 mA cm^{-2} at 0.0 V [the voltage is relative to the reversible hydrogen electrode (RHE), unless noted otherwise] and an onset potential of 0.35 V, if the onset potential is defined as the potential at 1.0 mA cm^{-2}. The chronoamperometry of the photocathode was measured for ≈181 h without noticeable degradation, specifically ≈108 at 0.0 V and 73 h at a maximum power point potential, $V_{mpp} = 0.16$ V.

2. Results and Discussion

2.1. 3D MoS_2 Film Growth on TiO_2/p-Si Photocathode Substrates

Figure 1a shows a schematic illustration of 3D MoS_2 films, directly deposited on the 4 in. TiO_2/p-Si photocathode substrates, by MOCVD using molybdenum hexacarbonyl (MHC), ($Mo(CO)_6$), and diethyl sulfide (DES), ($(C_2H_5)_2S$) precursors (see more details in the Experimental Section). In stark contrast with the conventional layer-by-layer growth of 2D MoS_2, this growth is characterized by 3D film morphology, where a large fraction of vertically aligned MoS_2 on the top of underlying MoS_2 polycrystalline films of a relatively small grain size of <10 nm (Figure 1a,b). This unique film texture was obtained at a higher flux rate growth, i.e., an MHC flow rate of 0.4 sccm and the DES rate of 8.5 sccm for 15 min. Figure 1c shows a plane view of a transmission electron microscopy (TEM) image, where the edge-exposed vertical MoS_2 few-layers coexist with the underlying MoS_2 films. The high-resolution TEM images, obtained from each region marked in Figure 1c, verify the corresponding vertical and in-plane crystal structures of few-layer MoS_2. The measured interplanar distances were 0.660 nm (Figure 1d) and 0.312 nm (Figure 1e), consistent with the (0001) and (10–10) plane of hexagonal MoS_2, respectively. The areal density of the vertical MoS_2 was estimated to be ≈50%, according to the representative scanning electron microscope image in Figure 1f and Figure S1 (Supporting Information). In Figure 1g, the in-plane dark-field TEM image with false colors, each of which corresponds to the in-plane crystal orientations, defined by diffraction patterns of Figure 1h, shows a polycrystalline grain distribution. Quantitatively, its grain size ranged from 2–20 nm (Figure 1i, green curve) with an average size of 8 nm by counting its size from more than five TEM images taken from the entire wafer—see also Figure S2 (Supporting Information) for the wafer-scale uniformity. In contrast, the lower flux rate growth at an MHC flow rate of 0.0001 sccm and the DES rate of 0.15 sccm establishes the conventional layer-by-layer growth mode without any vertical MoS_2 films, requiring 16 h to cover up the entire wafer (Figure S3, Supporting Information). In this growth mode, the typical grain size was found to be ≈60 nm (Figure 1i–k).

Evidently, the 3D film texture was achieved by growth kinetics controls in our MOCVD growth. For example, the higher precursor flow rate substantially increases the numbers of nucleation sites for MoS_2 embryos and the growth rate, resulting in smaller grains and various vertical textures in the growth products, respectively (Figure 1i and **Figure 2**a). Based on the cross-sectional TEM images as shown in, such 3D features were categorized into three types (Figure 2b–d; Figures S4 and Figure S5, Supporting Information): (i) the direct vertical growth on the top of either TiO_2 or the bottom MoS_2 layers, (ii) the second one occurs when the two propagating MoS_2 layers collide head-on, pushing them in the upright direction, and (iii) when the MoS_2 layers are bent and rolled over, presumably at the defect sites. The energy dispersive spectroscopy (EDS) mapping shows the clear distinction between the coated layer TiO_2 film and the 3D MoS_2 catalysts on p-Si as shown in Figure 2e. The uniform coverage of our 3D MoS_2 films was investigated by Raman scattering spectra (Figure 2f,g), obtained at various areas over the entire wafer. The representative Raman spectra obtained from the marked spots as [1] to [5] in Figure 2f consistently show two characteristic peaks of few-layer MoS_2, i.e., the in-plane vibrational E_{2g} mode in the range ≈380–381 cm^{-1} and the out-of-plane vibrational A_{1g} mode in the range ≈404–405 cm^{-1}. The frequency difference of the two peaks, $\Delta\omega$, which is strongly dependent on the layer number, was consistently observed to be in the range ≈23–25 cm^{-1} ($\Delta\omega \approx 19.5$ cm^{-1} for MoS_2 monolayer), indicating the nominal layer number is greater than 3 in our 3D films.[30,31] We also observed that the

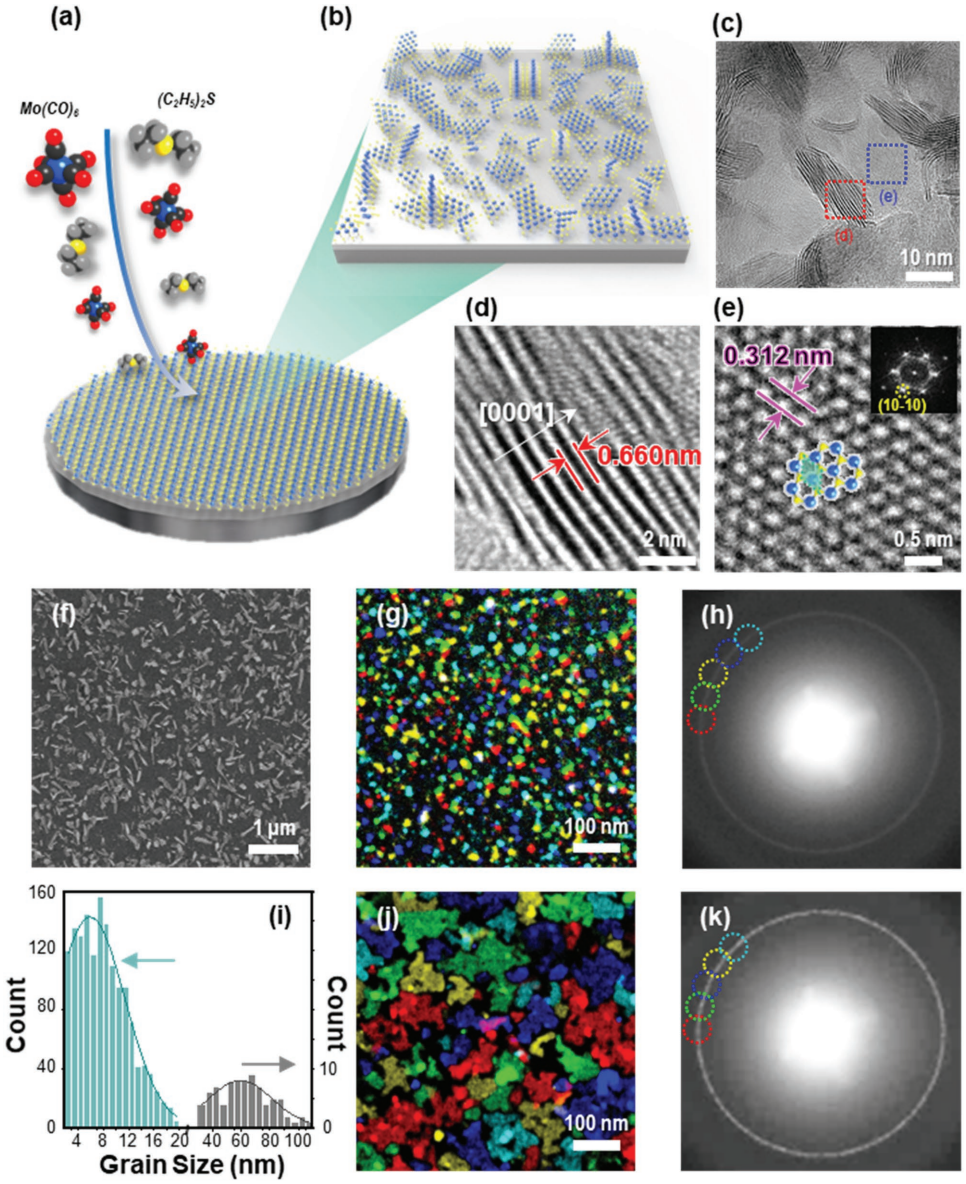

Figure 1. Wafer-scale 3D MoS_2 film growth by metal–organic chemical vapor deposition (MOCVD). a,b) Schematic illustration for direct growth of 3D MoS_2 film on 4 in. TiO_2/p-Si wafer by MOCVD. c) Low-magnification transmission electron microscope (TEM) image of 3D MoS_2 film. d,e) High-magnification TEM images of d) vertically aligned and e) in-planar region taken from marked areas in (c). f) Scanning electron microscope image, g) false-color dark-field-TEM (DF-TEM) image, and h) selected area electron diffraction (SAED) pattern taken from 3D MoS_2. i) Grain size distribution of 3D MoS_2 film (green) and layer-by-layer grown MoS_2 film (gray). j) False-color DF-TEM image and k) SAED pattern taken from layer-by-layer grown MoS_2.

E_{2g} peaks are weaker, compared to the A_{1g} peaks, with generic peak broadening, suggesting that the film is 3D-textured, instead of 2D monolayer or bilayer;[32] the full-width half-maximum (FWHM) was estimated to be 13.8 and 11.2 cm^{-1} for the E_{2g} and A_{1g} modes, respectively, while the FWHM in our monolayer films is 12.1 cm^{-1} (E_{2g}) and 8.4 cm^{-1} (A_{1g}).

Figure 3 shows the optical reflectance (R) of 3D MoS_2/TiO_2/p-Si and TiO_2/p-Si samples. The observed color contras in the photographic images of both 3D MoS_2/TiO_2/p-Si and TiO_2/p-Si specimens were an indication of the reduction of optical reflectance (Figure 3a,b). The absorption spectra and optical reflectance data of different MoS_2 growth time were summarized in Figure S6 (Supporting Information). The intensity of light absorption significantly increased with respect to increase of MoS_2 growth time. Furthermore, the dramatic reduction of reflectance with the 15 min grown 3D MoS_2/TiO_2/p-Si substrate is observed. For further analysis, the optical reflectance was measured in the wavelength (λ) range of 400–1000 nm at incident angle (θ) range of 10°–70° and confirmed that the 3D MoS_2 films decreased reflectance of the bare sample (Figure 3c,d). Moreover, the arithmetic mean of the R versus λ at $\theta = 40°$ and the R versus θ measured at $\lambda = 550$ nm are found to be 35.2% and 34.0% for the TiO_2/p-Si and 21.9% and 21.9% for the 3D MoS_2/TiO_2/p-Si photocathode, respectively (Figure 3e,f). The

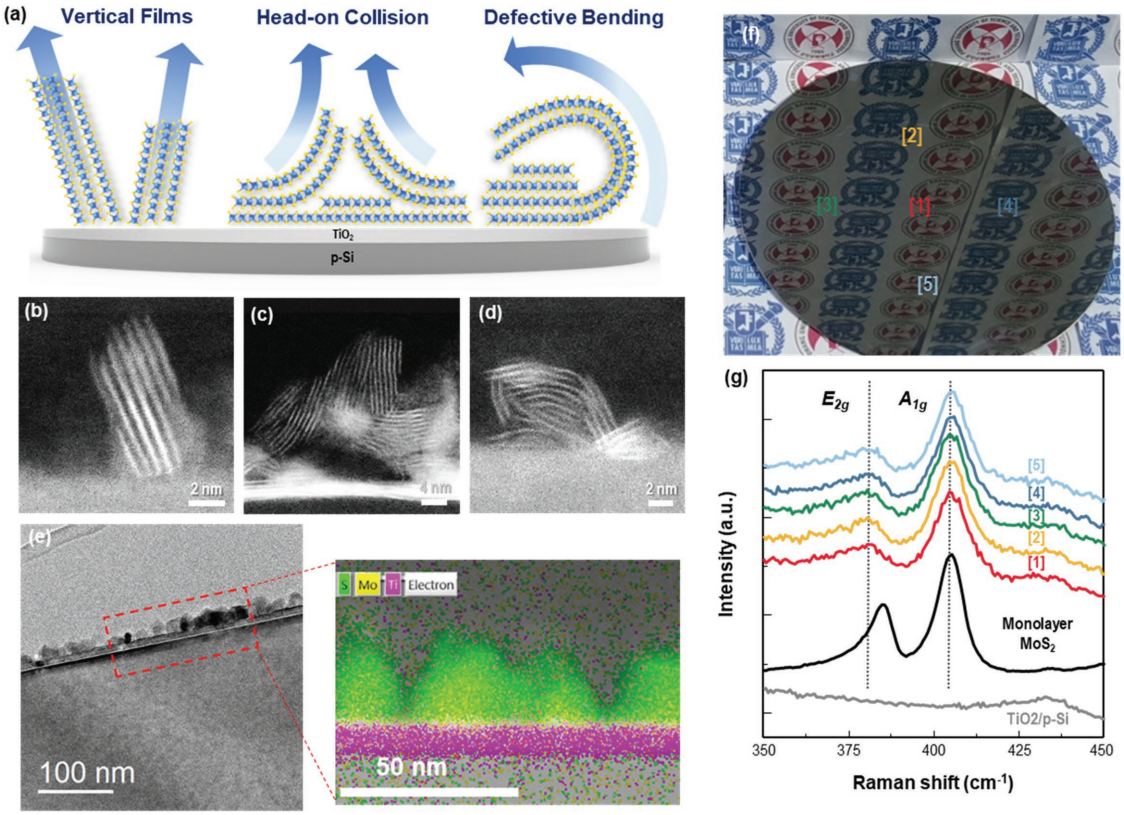

Figure 2. Vertically aligned 3D MoS_2 film with exposed edge by kinetic control. a) Schematic illustration of vertically aligned textures observed in 3D MoS_2 films at high precursor flux rate. b–d) Representative cross-sectional high-angle annular dark field-scanning TEM (HAADF-STEM) images showing different growth features. e) TEM image of 3D MoS_2 films and EDS mapping of the specimens (inset). f) Photograph of 3D MoS_2 film grown on 4 in. TiO_2/p-Si substrate. g) Raman scattering spectra acquired from different regions in (f) with those of monolayer MoS_2 film (black) and TiO_2/p-Si (gray) for comparison.

θ- and λ-dependent R of both the samples are smaller than that of the pristine TiO_2/p-type Si because of a gradient refractive index, 2.545/2.64/5.6.[33,34] The refractive index of the 3D MoS_2 structures covering 50% of the TiO_2/p-Si area was estimated to 2.545, considering the refractive index of the MoS_2 in parallel direction and areal density.[35,36] More importantly, in the 3D MoS_2/TiO_2/p-Si photocathode, the variation of R in both R versus θ and R versus λ is negligible, indicating that the 3D MoS_2 film has omnidirectional and broadband antireflective properties for p-Si, presumably because of the size effect below the diffraction limit.[37]

2.2. Photoelectrochemical Performance

Figure 4a shows the linear sweep voltammograms (LSV) of our 3D MoS_2/TiO_2/p-Si (red color), 2D layered MoS_2/TiO_2/p-Si (blue color), and TiO_2/p-Si (black color) photocathodes. The saturation current density of the 3D MoS_2/TiO_2/p-Si is ≈37 mA cm^{-2}, whereas it was 33 and 32 mA cm^{-2} for the layered MoS_2/TiO_2/p-Si and TiO_2/p-Si, respectively. The enhanced saturation photocurrent density of MoS_2/TiO_2/p-Si photocathodes is due to the decrease of the R that increases the charge generation efficiency of the photocathode. The electrochemical performance of 3D MoS_2/TiO_2/glassy carbon electrode was demonstrated in Figure S7 (Supporting Information). The overpotential at 10 mA cm^{-2} is –0.255 V and the Tafel slope of fabricated cell is 87.01 mV dec^{-1}. The chronopotentiometry of both 2D and 3D MoS_2/TiO_2/p-Si photocathodes at 1.00 mA cm^{-2} was measured using chopped light as shown in Figure 4b. The onset potential of TiO_2/p-Si photocathode was found to be –0.41 V, whereas it was 0.2 and 0.35 V for the 2D MoS_2/TiO_2/p-Si and 3D MoS_2/TiO_2/p-Si, respectively, assuming that the onset potential of the photocathode is the potential at which the photocathode can generate a current density of 1.00 mA cm^{-2}. The onset potential of 3D MoS_2/TiO_2/p-Si photocathode shifted anodically by 0.76 and 0.15 V relative to those of TiO_2/p-Si and 2D MoS_2/TiO_2/p-Si photocathode, respectively, whereas it anodically shifted by 0.61 V for 2D MoS_2/TiO_2/p-Si photocathode, compared to that of the pristine TiO_2/p-Si photocathode. The high anodic onset potential shift in the 3D MoS_2/TiO_2/p-Si photocathode can be attributed to the existence of MoS_2 edge sites in high density and much smaller size of grain boundaries, lacking in the 2D layered MoS_2/TiO_2/p-Si photocathode. A comparison of the PEC performance between the 3D MoS_2/TiO_2/p-Si photocathode and the state-of-the-art photocathodes reported using similar catalytic and optical absorption materials is shown in Figure S8 (Supporting Information). Because of the highly populated edge-sites, the potential of our photocathodes at

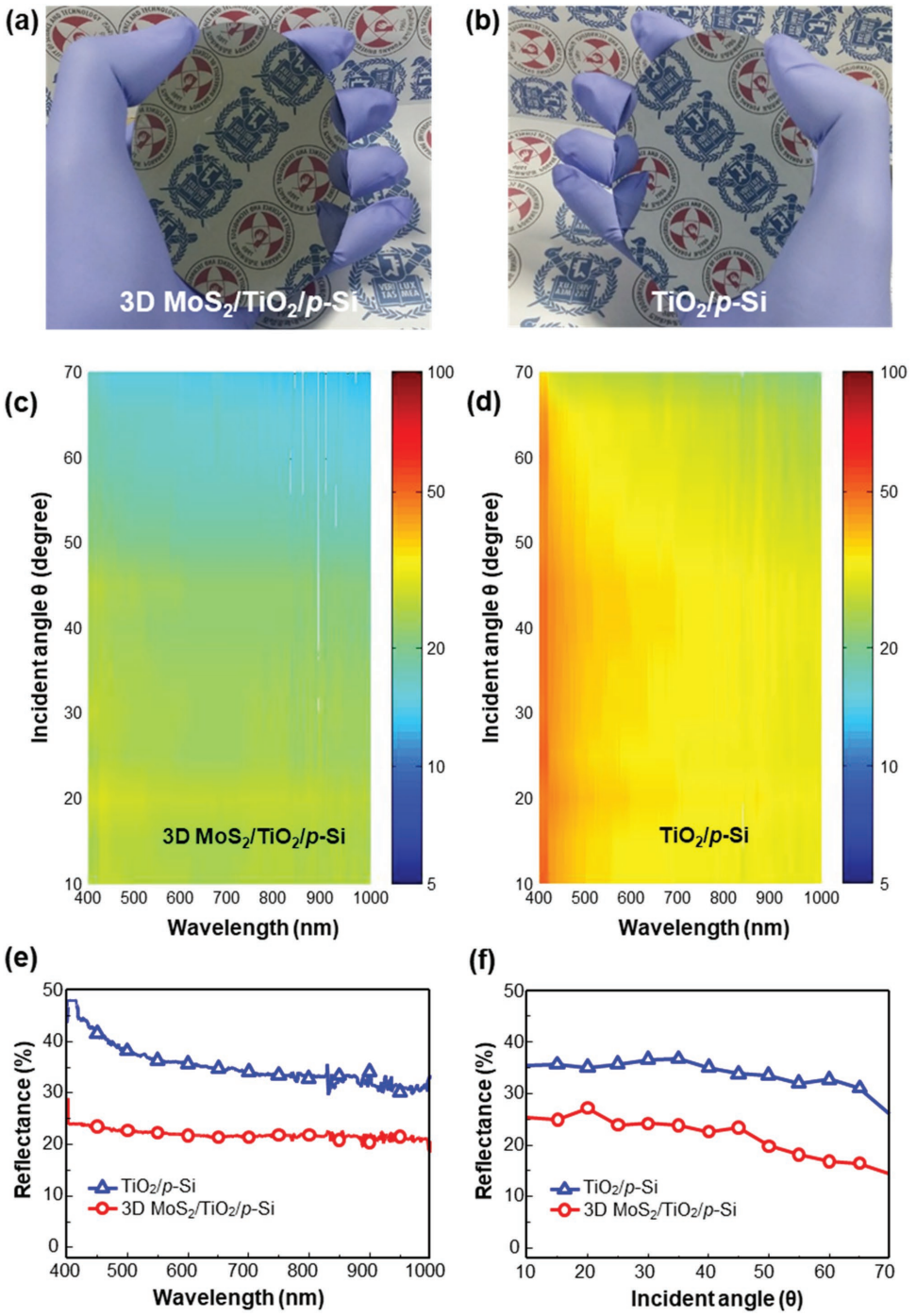

Figure 3. Optical reflectance of the specimens. a,b) Photograph of 3D MoS_2 film on TiO_2/p-Si and TiO_2 films on p-Si substrate. c,d) Reflectance of 3D MoS_2/TiO_2/p-Si and TiO_2/p-Si specimens. e) Reflectance spectra of 3D MoS_2/TiO_2/p-Si (red) and TiO_2/p-Si (blue) at the incident angle 40°. f) Reflectance versus incident angle at the wavelength of 550 nm irradiation.

1 mA cm^{-2} is comparable with those of the previously reported photocathodes which are $MoS_x/MoS_2/Mo/n^+$p-Si,[38] MoS_2/Ti/n^+p-Si,[39] $[Mo_3S_{13}]^{2-}/MoS_2/Mo/n^+$p-Si[40] or $MoS_2/Al_2O_3/n^+$p-Si.[41] For the saturation current density and the current density at zero bias voltage, our photocathode shows the highest photocurrent density, mostly because of the improvement of charge generation efficiency and lower interfacial charge resistance.

Electrochemical impedance spectroscopy (EIS) measurements were performed to deduce the charge transfer resistance of the 3D MoS_2/TiO_2/p-Si and TiO_2/p-Si photocathodes. The Nyquist impedance plots are shown in Figure 4c, where the TiO_2/p-Si photocathode has a greater diameter than 3D MoS_2/TiO_2/p-Si. The fitted equivalent circuit of the Nyquist plot consists of a constant phase element and resistances such as series

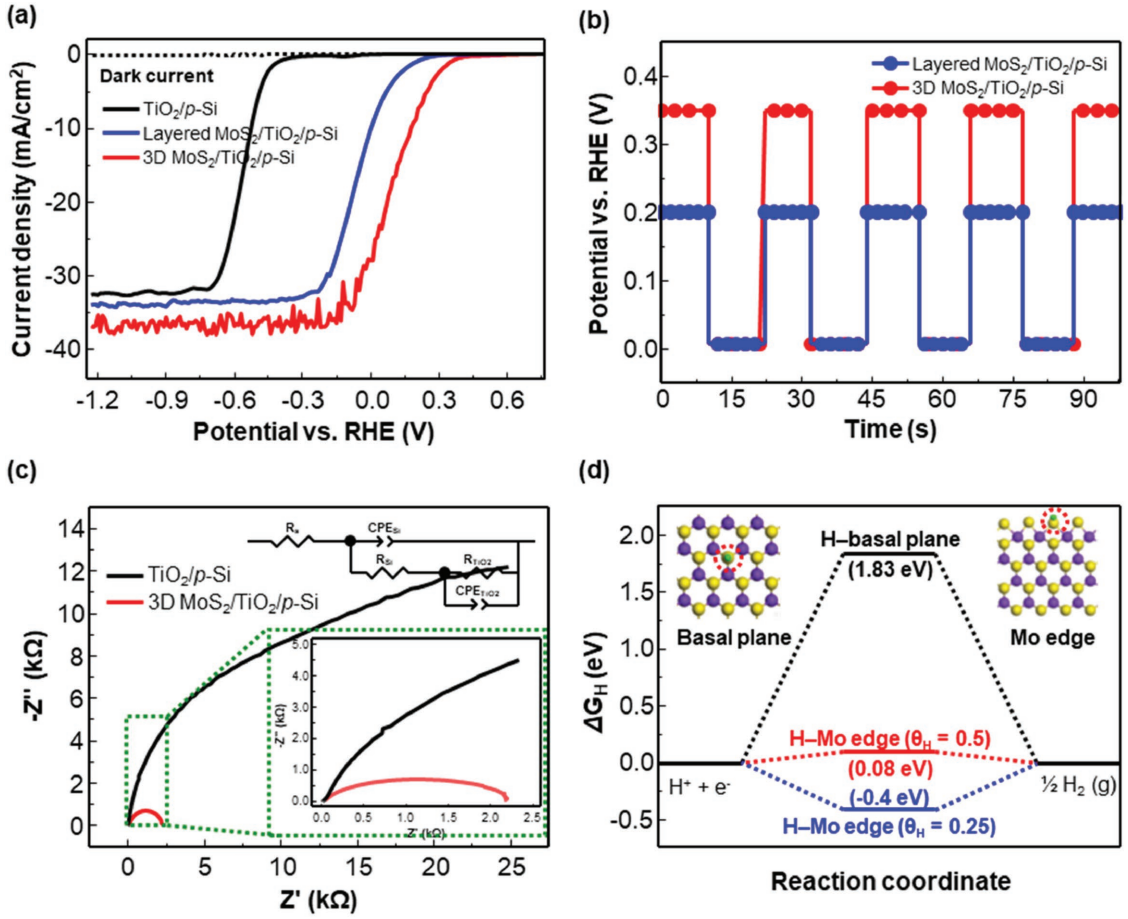

Figure 4. The PEC performance of the working electrodes, MoS_2/TiO_2/p-Si, TiO_2/p-Si, and bare Si photocathode. a) The LSV of MoS_2/TiO_2/p-Si and TiO_2/p-Si. b) The onset potential of layered and 3D MoS_2/TiO_2/p-Si at –1 mA cm^{-2}. c) Nyquist plots of the working electrodes 3D MoS_2/TiO_2/p-Si and TiO_2/p-Si d) hydrogen adsorption free energy of MoS_2 basal plane, Mo edge calculated using DFT.

resistance (R_s), charge transfer resistance from silicon to TiO_2 (R_{Si}), and charge transfer resistance from TiO_2 to electrolyte through MoS_2 (R_{TiO2}), as shown in the inset of Figure 4c. The fitted charge transfer resistances of the photocathodes are listed in **Table 1**, where the charge transfer resistance from silicon to TiO_2 was almost equal for both the photocathodes, 3D MoS_2/TiO_2/p-Si and TiO_2/p-Si, which are 45 and 40 Ω cm^2, respectively. However, the charge transferred resistance from TiO_2 to electrolyte through a MoS_2 was found to be quite small compared to the charge transferred resistance from TiO_2 to electrolytes, which were 128 and 634 Ω cm^2 for 3D MoS_2/TiO_2/p-Si and TiO_2/p-Si photocathode, respectively. To clarify the electron transport in fabricated samples, the ultraviolet photoemission spectroscopy and X-ray photoemission spectroscopy valence spectra were conducted as shown in Figure S9 (Supporting Information). Based on these results, the energy band diagram clearly shows that the photogenerated electrons from p-Si can be effectively transported to the TiO_2 and 3D MoS_2 layers. Furthermore, the holes from the photogenerated carriers were blocked by TiO_2 thin films due to its valence band position, indicating that the recombination of photogenerated carriers is inhibited as shown in Figure S9 (Supporting Information).

The Gibbs free energy of hydrogen adsorption (ΔG_H) on the basal plane and edge sites of MoS_2 was calculated using density functional theory (DFT) to support the experimental results, because Gibbs free energy is considered as a descriptor for HER efficiency (see the Experimental Section for detail of the DFT calculation).[42–45] The Gibbs free energy of hydrogen adsorption closer to zero indicates the highest catalytic activities of the material for HER.[21] The ΔG_H on the H–Mo edge was considered, because more than half of the 3D MoS_2 surfaces are covered by exposed edges of MoS_2 (Figures 1c,d and 3b–d). For a hydrogen coverage θ_H, 0.5 and 0.25 were considered. Figure 4d shows the calculated results of ΔG_H for MoS_2 on the basal plane and Mo edges. On the basal plane of MoS_2, the ΔG_H was found to be thermodynamically unstable (1.83 eV), indicating that the basal plane is inert for HER. The ΔG_H on the Mo edge sites with 0.5 and 0.25 hydrogen coverage was

Table 1. The fitted charge transfer resistance.

Photocathode	R_{Si} [Ω cm^2]	R_{TiO2} [Ω cm^2]	Appl. volt versus OCP
TiO_2/p-Si	40.7	4634.4	340 mV
MoS_2/TiO_2/p-Si	45.3	128	340 mV

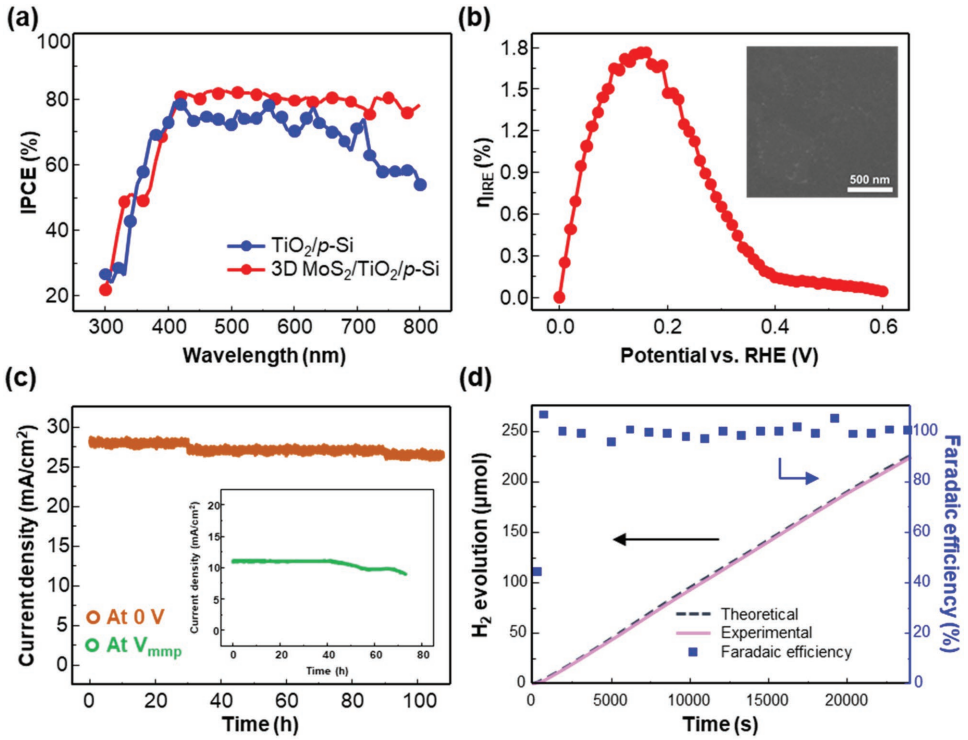

Figure 5. Efficiency and stability of the photocathode. a) IPCE curves of 3D MoS_2/TiO_2/p-Si and TiO_2/p-Si. b) Ideal regenerative cell efficiency of 3D MoS_2/TiO_2/p-Si. c) Stability of photocathode, 3D MoS_2/TiO_2/p-Si at zero versus RHE bias potential and at the maximum power point potential V_{mpp}. The inset shows an SEM image of 3D MoS_2/TiO_2/p-Si after measurement of photoelectrochemical properties. d) Calculated amounts of H_2 evolution of theoretical and experimental (left axis), and Faradaic efficiency measurements under illumination at –0.05 V versus RHE (right axis).

0.08 and –0.4 eV, respectively. The obtained ΔG_H values validated the experimental result of EIS and LSV analysis of 3D MoS_2/TiO_2/p-Si photocathode.

The incident photon-to-current conversion efficiency (IPCE) of 3D MoS_2/TiO_2/p-Si and TiO_2/p-Si samples was measured at a bias voltage of 0.0 and –0.65 V, respectively, as shown in **Figure 5**a. The IPCE of the photocathodes are ≈85 and 75% for 3D MoS_2/TiO_2/p-Si and TiO_2/p-Si, respectively, in the entire visible light spectrum. The ideal regenerative cell efficiency[46] of the 3D MoS_2/TiO_2/p-Si photocathode was measured, as shown in Figure 5b. The photocathode exhibited V_{mpp} = 0.16 V photovoltage and J_{mpp} = 11.06 mA cm^{-2} current density at the maximum power point. The ideal regenerative cell efficiency of the photocathode was found to be 1.8%.

Figure 5c shows the measured chronoamperometry of 3D MoS_2/TiO_2/p-Si photocathode for an extended time at a bias potential of 0.0 V and the maximum power point potential (V_{mpp} = 0.16 V) to elucidate the stability for more than 108 h (brown color curve) at 0.0 V versus RHE and ≈73 h (green color curve) at the maximum power point bias voltage. To elucidate the passivation effect of 3D MoS_2 on the TiO_2/p-Si photocathodes, we measured the chronoamperometry curve for the fabricated samples which are bare p-Si, TiO_2/p-Si and 3D MoS_2/TiO_2/p-Si photocathodes as shown in Figure S10 (Supporting Information). The TiO_2/p-Si photocathode exhibited the gradual degradation (63% of initial photocurrent density after 10 000 s) compared to the bare p-Si (13% of initial photocurrent density after 10 000 s) which showed rapid degradation. The TiO_2 thin film used in this study was only 10 nm, it is not sufficient to passivate the p-Si photocathode during the PEC measurements in the acidic condition. However, for the 3D MoS_2 deposited TiO_2/p-Si photocathode, the photocurrent density was stable after 10 000 s without notable degradation, indicating that the 3D MoS_2 acts as not only a catalyst for hydrogen production but also an excellent passivation layer. For the electrochemical stability, we have investigated the stability of the 3D MoS_2/TiO_2/glassy carbon(GC) by continuous cyclic voltammetry for 3000 cycles at a constant scanning rate of 100 mV s^{-1}. Comparing the first cycle of the samples with the final one, there is no obvious change in the polarization curve, indicating that 3D MoS_2 is a superior stable HER electrocatalyst. The prolonged time stability of 3D MoS_2/TiO_2/p-Si photocathode is attributed to the MoS_2 nanostructure that serves as a passivation of the TiO_2/p-Si electrode. The spillover of hydrogen from the surface of 3D MoS_2/TiO_2/p-Si and TiO_2/p-Si photocathode at 0.0 V is recorded and shown in the Videos S1 and S2 (Supporting Information). The H_2 evolution of 3D MoS_2/TiO_2/p-Si photocathode is measured by gas chromatography at –0.05 V versus RHE. The blue-colored dots in Figure 5d display ≈100% Faradaic efficiency over 8 h. The calculated amounts of H_2 evolution are very close to that of theoretical value according to the passed charge, indicating that the most of the photogenerated charges are consumed for H_2 evolution reaction not for other side reaction.

3. Conclusion

We successfully demonstrated an efficient TiO_2 coated 4 in. p-Si photocathode with a directly grown 3D MoS_2 HER catalyst. The photoelectrochemical performance of the photocathode for a 3D MoS_2/TiO_2/p-Si exhibited the onset potential of 0.35 V with the short-circuit current density J_{sc} = 28 mA cm^{-2} and the saturated current density of 37 mA cm^{-2}; for the layered MoS_2/TiO_2/p-Si photocathode, the onset potential was 0.2 V at a J_{sc} = 10 mA cm^{-2} and a saturated current density of 33 mA cm^{-2}. The onset potential of the 3D MoS_2/TiO_2/p-Si photocathode shifted anodically by 0.76 V relative to the onset potential of the pristine TiO_2/p-Si photocathode. Passivation of the TiO_2/p-Si photocathodes with MoS_2 layers secured the stable operation for ≈181 h without noticeable degradation. The obtained high anodic shift in the 3D MoS_2/TiO_2/p-Si photocathode is attributed to the high density of exposed edge sites and grain boundaries. The enhanced saturation current of the photocathode resulted from the decrease in optical reflectance. Our work can pave a way in the development of efficient catalysts for the PEC hydrogen evolution reactions.

4. Experimental Section

TiO_2 Coating on a p-Type Silicon Substrate: A p-type Si (100) substrate was cleaned using acetone and isopropanol alcohol assisting with sonication, and washed repeatedly in deionized water (DI) water. Subsequently, it was soaked in 2% HF for 1 min to remove residues and native oxides and was washed in DI water. Then, a 10 nm thick TiO_2 film was deposited at a rate of 0.1 Å sec^{-1} using an electron-beam evaporator (KVE-E2004L) at 3.5×10^{-6} Torr.

Growth Methods of 3D MoS_2 Layers in Wafer Scale: The 4 in. wafer-scale growth of MoS_2 films was carried out using high purity gas precursor MHC (99.9%) and DES (98%). A 4 in. TiO_2 (10 nm) coated p-Si wafer is located in the center of a hot-walled quartz-tube furnace. Prior to heating, the furnace was purged for 30 min to eliminate residual gases, and subsequently was ramped up to 560 °C for 20 min. Then, the precursors and a carrier gas were flowed. The growth was proceeded for 15 min and was rapidly cooled down to room temperature. The flow rates of precursors were 0.4 sccm for MHC, 8.5 sccm for DES, 20 sccm for H_2 (99.9999%), and 150 sccm for Ar (99.9999%).

TEM Characterizations: For TEM specimen preparations, 3D MoS_2 was transferred using a wet transfer method. The grown sample was spin-coated by poly(methyl methacrylate) (PMMA) and baked at 180 °C for 1 m and 30 s. Then, substrate (SiO_2) was etched in HF (10%). Floating PMMA/samples were transferred to a TEM grid (holey carbon coated with 400 meshed Cu), and then, PMMA films were removed in acetone for 6 h and annealed in a tube furnace at 300 °C. High-resolution TEM analysis was taken using a JEOL JEM-2100F operated at 200 kV (equipped with a Cs-corrector).

Photoelectrochemical Measurement: The photoelectrochemical properties of the photocathode were measured using a computer controlled potentiostat (IVIUM Technologies, nSTAT). All the PEC measurements were performed with a 0.5 M H_2SO_4 electrolyte, single compartment cuvette, and three electrodes configuration, such as, the prepared photocathode, saturated calomel electrode, and graphite rod as working, reference, and counter electrode, respectively. A Xe arc lamp was used as a light source and calibrated to 100 mW cm^{-2} using a standard silicon photodiode at the sample location. In all of the linear sweep voltammogram measurements, the photoanodes were cathodically polarized at the scan rate of 20 mV sec^{-1} during both illumination and in the dark measurement. The measured potential V versus calomel were converted to reference hydrogen electrode (RHE) using the following Equation (1)

$$V_{RHE} = E + E_{calomel} + 0.059 \times pH \quad (1)$$

where E is applied potential versus calomel and calomel is 0.24 V versus RHE and V_{RHE} is the applied bias potential versus RHE. The external quantum efficiency of the samples was measured at applied bias potential versus calomel using computer controlled monochromator (MonoRa150) and an amplifier for photocurrent detection. The EIS was measured at 0.0 V versus calomel with respect to open-circuit potential (OCP) and sweeping in the frequency range of 350 kHz–0.1 Hz with an AC amplitude of 10 mV. The EIS Nyquist curves were fitted to equivalent circuit using Z-plot 2x software. The Faradaic efficiency was measured by two-compartment photoelectrochemical cells which are separated by the Nafion 117 membrane. Before reaction, the two compartments of the reactor were degassed by bubbling with Ar gas for 30 min. During the reaction, the Ar gas was continuously flowed into electrolyte in the cathodic compartment with a rate of 10 sccm and vented directly into a gas-sampling loop of a gas chromatography measurement system (Agilent GC 7890B), which is equipped with a thermal conductivity detector and a micropacked column (ShinCarbon ST 100/120). The Ar gas was used as the carrier gas and the evolved H_2 was detected by thermal conductivity detector. A gas sample was analyzed automatically every 20 min.

DFT Calculations: DFT calculations were performed by a projector augmented wave method,[47] with Vienna Ab initio Simulation Package (VASP).[48,49] The generalized gradient approximation suggested by Perdew, Burke, and Ernzrh[50,51] was used for exchange correlation function. Van der Waals force was considered by the Grimme D2 scheme.[52] The basal plane was modeled as 4 × 4 × 1 single layer supercell, and the unit cell for the Mo-edge site was modeled by stripe with 5 Mo atoms in both the x- and y-direction as shown in Figure 4d inset. Two types of Mo-edges exist in MoS_2; one terminated with S-monomer and the other terminated with S-dimer. It is known in previous researches that hydrogens are absorbed on Mo-edge terminated with S-monomer,[53] so only one with S-monomer was calculated. The vacuum region was implemented as 15 Å thickness and used to avoid spurious electrostatic interactions. The plane-wave cutoff energy of 260 eV was used. The Brillouine zone was sampled by 5 × 5 × 1 Monkhorst-Pack mesh for unit cell, 2 × 2 × 1 for the basal plane, and 4 × 4 × 1 for the Mo-edge site. Gibbs free energy of the adsorption was obtained as follows

$$\Delta G_H = \Delta E_H + ZPE - T\Delta S_H \quad (2)$$

where ΔE_H is hydrogen adsorption energy, ZPE is zero-point energy, T is the temperature, and ΔS_H is entropy change on H adsorption. The entropy is only considered for hydrogen gas. Coverage of hydrogen θ was defined as the proportion of S-monomers at which hydrogen atoms are attached. Adsorption energy ΔE_H was calculated using following equation

$$\Delta E_H = E(*n\mathrm{H}) - E(*(n-1)\mathrm{H}) - \tfrac{1}{2}E(\mathrm{H_2}) \quad (3)$$

where $E(*n\mathrm{H})$ is the total energy of MoS_2 system that n edge sites are covered with hydrogen, and $E(H_2)$ is the total energy of a hydrogen molecule.

Supporting Information

Supporting Information is available from the Wiley Online Library or from the author.

Acknowledgements

D.M.A., G.J., C.-S.L., and C.K. contributed equally to this work. D.M.A., C.K., K.C.K., S.C., W.S., C.W.M., J.M.S., S.K., S.H., and H.W.J. were supported by the Samsung Research Funding Center of Samsung

Electronics under the project number SRFC-MA1402-13, and G.J., C.-S.L., J.P., H.H., and M.-H.J. were supported by the Institute for Basic Science (IBS), Korea under the Project Code (IBS-R014–A1).

Conflict of Interest

The authors declare no conflict of interest.

Keywords

3D molybdenum disulfide, antireflection, hydrogen evolution reaction catalysts, metal–organic chemical vapor deposition, solar water splitting

Received: October 2, 2017
Revised: November 27, 2017
Published online:

[1] A. Fujishima, K. Honda, *Nature* **1972**, *238*, 37.
[2] M. Liu, Y. Chen, J. Su, J. Shi, X. Wang, L. Guo, *Nat. Energy* **2016**, *1*, 16151.
[3] X. Zou, Y. Zhang, *Chem. Soc. Rev.* **2015**, *44*, 5148.
[4] D. M. Andoshe, J.-M. Jeon, S. Y. Kim, H. W. Jang, *Electron. Mater. Lett.* **2015**, *11*, 323.
[5] Z. Chen, D. Cummins, B. N. Reinecke, E. Clark, M. K. Sunkara, T. F. Jaramillo, *Nano Lett.* **2011**, *11*, 4168.
[6] H. I. Karunadasa, E. Montalvo, Y. Sun, M. Majda, J. R. Long, C. J. Chang, *Science* **2012**, *335*, 698.
[7] Z. Sun, H. Zheng, J. Li, P. Du, *Energy Environ. Sci.* **2015**, *8*, 2668.
[8] F. Urbain, V. Smirnov, J.-P. Becker, A. Lambertz, F. Yang, J. Ziegler, B. Kaiser, W. Jaegermann, U. Rau, F. Finger, *Energy Environ. Sci.* **2016**, *9*, 145.
[9] T. Bak, J. Nowotny, M. Rekas, C. Sorrell, *Int. J. Hydrogen Energy* **2002**, *27*, 991.
[10] L. Ji, M. D. McDaniel, S. Wang, A. B. Posadas, X. Li, H. Huang, J. C. Lee, A. A. Demkov, A. J. Bard, J. G. Ekerdt, E. T. Yu, *Nat. Nanotechnol.* **2015**, *10*, 84.
[11] D. M. Andoshe, S. Choi, Y.-S. Shim, S. H. Lee, Y. Kim, C. W. Moon, D. H. Kim, S. Y. Lee, T. Kim, H. K. Park, M. G. Lee, J.-M. Jeon, K. T. Nam, M. Kim, J. K. Kim, J. Oh, H. W. Jang, *J. Mater. Chem. A* **2016**, *4*, 9477.
[12] Q. Ding, F. Meng, C. R. English, M. Cabán-Acevedo, M. J. Shearer, D. Liang, A. S. Daniel, R. J. Hamers, S. Jin, *J. Am. Chem. Soc.* **2014**, *136*, 8504.
[13] M. A. Lukowski, A. S. Daniel, F. Meng, A. Forticaux, L. Li, S. Jin, *J. Am. Chem. Soc.* **2013**, *135*, 10274.
[14] A. B. Laursen, S. Kegnæs, S. Dahl, I. Chorkendorff, *Energy Environ. Sci.* **2012**, *5*, 5577.
[15] B. Hinnemann, P. G. Moses, J. Bonde, K. P. Jørgensen, J. H. Nielsen, S. Horch, I. Chorkendorff, J. K. Nørskov, *J. Am. Chem. Soc.* **2005**, *127*, 5308.
[16] Z. M. Wang, *MoS2: Materials, Physics, and Devices*, Vol. *21*, Springer Science & Business Media, NY, USA **2013**.
[17] W. Zhao, R. M. Ribeiro, M. Toh, A. Carvalho, C. Kloc, A. Castro Neto, G. Eda, *Nano Lett.* **2013**, *13*, 5627.
[18] Q. Ding, B. Song, P. Xu, S. Jin, *Chem* **2016**, *1*, 699.
[19] Y. Yin, Y. Zhang, T. Gao, T. Yao, X. Zhang, J. Han, X. Wang, Z. Zhang, P. Xu, P. Zhang, X. Cao, B. Song, S. Jin, *Adv. Mater.* **2017**, *29*, 1700311.
[20] Y. Yin, J. Han, Y. Zhang, X. Zhang, P. Xu, Q. Yuan, L. Samad, X. Wang, Y. Wang, Z. Zhang, P. Zhang, X. Cao, B. Song, S. Jin, *J. Am. Chem. Soc.* **2016**, *138*, 7965.
[21] H. Li, C. Tsai, A. L. Koh, L. Cai, A. W. Contryman, A. H. Fragapane, J. Zhao, H. S. Han, H. C. Manoharan, F. Abild-Pedersen, J. K. Nørskov, X. Zheng, *Nat. Mater.* **2016**, *15*, 48.
[22] A. Haas, *Angew. Chem., Int. Ed.* **1965**, *4*, 1014.
[23] M. Chhowalla, H. S. Shin, G. Eda, L.-J. Li, K. P. Loh, H. Zhang, *Nat. Chem.* **2013**, *5*, 263.
[24] K. C. Kwon, S. Choi, K. Hong, C. W. Moon, Y.-S. Shim, D. H. Kim, T. Kim, W. Sohn, J.-M. Jeon, C.-H. Lee, K. T. Nam, S. Han, S. Y. Kim, H. W. Jang, *Energy Environ. Sci.* **2016**, *9*, 2240.
[25] Z. Lin, Y. Zhao, C. Zhou, R. Zhong, X. Wang, Y. H. Tsang, Y. Chai, *Sci. Rep.* **2015**, *5*, 18596.
[26] D. Ma, J. Shi, Q. Ji, K. Chen, J. Yin, Y. Lin, Y. Zhang, M. Liu, Q. Feng, X. Song, X. Guo, J. Zhang, Y. Zhang, Z. Liu, *Nano Res.* **2015**, *8*, 3662.
[27] Z. Lu, L. Sun, G. Xu, J. Zheng, Q. Zhang, J. Wang, L. Jiao, *ACS Nano* **2016**, *10*, 5237.
[28] Q. Ding, J. Zhai, M. Cabán-Acevedo, M. J. Shearer, L. Li, H. C. Chang, M. L. Tsai, D. Ma, X. Zhang, R. J. Hamers, J.-H. He, S. Jin, *Adv. Mater.* **2015**, *27*, 6511.
[29] X. Zhang, F. Meng, S. Mao, Q. Ding, M. J. Shearer, M. S. Faber, J. Chen, R. J. Hamers, S. Jin, *Energy Environ. Sci.* **2015**, *8*, 862.
[30] Y. Zhan, Z. Liu, S. Najmaei, P. M. Ajayan, J. Lou, *Small* **2012**, *8*, 966.
[31] H. Li, Q. Zhang, C. C. R. Yap, B. K. Tay, T. H. T. Edwin, A. Olivier, D. Baillargeat, *Adv. Funct. Mater.* **2012**, *22*, 1385.
[32] D. Kong, H. Wang, J. J. Cha, M. Pasta, K. J. Koski, J. Yao, Y. Cui, *Nano Lett.* **2013**, *13*, 1341.
[33] D. E. Aspnes, A. A. Studna, *Phys. Rev. B* **1983**, *27*, 985.
[34] J. R. DeVore, *J. Opt. Soc. Am.* **1951**, *41*, 416.
[35] K. Pandey, P. Yadav, D. Singh, S. K. Gupta, Y. Sonvane, I. Lukačević, J. Kim, M. Kumar, *Sci. Rep.* **2016**, *6*, 32690.
[36] L. Fanni, B. Delaup, B. Niesen, Y. Milstein, D. Shachal, M. Morales-Masis, S. Nicolay, C. Ballif, *Mater. Res. Express* **2015**, *2*, 075006.
[37] G.-J. Lim, H.-P. Wang, D.-H. Lien, P.-H. Fu, H.-C. Chang, C.-H. Ho, C.-A. Lin, K.-Y. Lai, J.-H. He, *Nano Energy* **2014**, *6*, 36.
[38] A. B. Laursen, T. Pedersen, P. Malacrida, B. Seger, O. Hansen, P. C. Vesborg, I. Chorkendorff, *Phys. Chem. Chem. Phys.* **2013**, *15*, 20000.
[39] B. Seger, A. B. Laursen, P. C. Vesborg, T. Pedersen, O. Hansen, S. Dahl, I. Chorkendorff, *Angew. Chem., Int. Ed.* **2012**, *51*, 9128.
[40] J. D. Benck, S. C. Lee, K. D. Fong, J. Kibsgaard, R. Sinclair, T. F. Jaramillo, *Adv. Energy Mater.* **2014**, *4*, 1400739.
[41] R. Fan, J. Mao, Z. Yin, J. Jie, W. Dong, L. Fang, F. Zheng, M. Shen, *ACS Appl. Mater. Interfaces* **2017**, *9*, 6123.
[42] R. Parsons, *Trans. Faraday Soc.* **1958**, *54*, 1053.
[43] S. Trasatti, *J. Electroanal. Chem. Interfacial Electrochem.* **1971**, *33*, 351.
[44] J. K. Nørskov, T. Bligaard, A. Logadottir, J. Kitchin, J. G. Chen, S. Pandelov, U. Stimming, *J. Electrochem. Soc.* **2005**, *152*, J23.
[45] J. Greeley, T. F. Jaramillo, J. Bonde, I. Chorkendorff, J. K. Nørskov, *Nat. Mater.* **2006**, *5*, 909.
[46] R. H. Coridan, A. C. Nielander, S. A. Francis, M. T. McDowell, V. Dix, S. M. Chatman, N. S. Lewis, *Energy Environ. Sci.* **2015**, *8*, 2886.
[47] G. Kresse, D. Joubert, *Phys. Rev. B* **1999**, *59*, 1758.
[48] G. Kresse, J. Furthmüller, *Comput. Mater. Sci.* **1996**, *6*, 15.
[49] G. Kresse, J. Furthmüller, *Phys. Rev. B* **1996**, *54*, 11169.
[50] J. P. Perdew, K. Burke, M. Ernzerhof, *Phys. Rev. Lett.* **1996**, *77*, 3865.
[51] J. P. Perdew, M. Ernzerhof, *J. Chem. Phys.* **1996**, *105*, 9982.
[52] S. Grimme, *J. Comput. Chem.* **2006**, *27*, 1787.
[53] M. Bollinger, K. W. Jacobsen, J. K. Nørskov, *Phys. Rev. B* **2003**, *67*, 085410.

